INORGANIC CHEMISTRY FRONTIERS

CCS 中国化学会 CHINESE CHEMICAL SOCIETY

ROYAL SOCIETY OF CHEMISTRY

Observing the Three-Dimensional Dynamics of Supported Metal Complexes

Journal:	*Inorganic Chemistry Frontiers*
Manuscript ID	QI-RES-10-2020-001241.R2
Article Type:	Research Article
Date Submitted by the Author:	23-Dec-2020
Complete List of Authors:	Perras, Frédéric A.; Ames Laboratory, Chemical and Biological Sciences Paterson, Alexander L.; Ames Laboratory, Liu, Da-Jiang; Iowa State University, Ames Laboratory Kanbur, Uddhav; Iowa State University, Department of Chemistry Sadow, Aaron; Iowa State University, Department of Chemistry

Observing the Three-Dimensional Dynamics of Supported Metal Complexes

Alexander L. Paterson,[1] Da-Jiang Liu,[1] Uddhav Kanbur,[1,2] Aaron D. Sadow,[1,2] Frédéric A. Perras[1]*

[1]US DOE, Ames Laboratory, Ames, IA 50011 USA
[2]Department of Chemistry, Iowa State University, Ames, IA 50011 USA

*Author to whom correspondence should be addressed
fperras@ameslab.gov

Abstract

Dynamics are intricately linked with activity and selectivity when it comes to catalysis, as noted for instance in the enzymatic principles of induced fit and allostery, and yet the range of motions heterogeneous catalytic sites are able to undergo is poorly understood. Solid-state nuclear magnetic resonance (NMR) spectroscopy is perhaps the only tool capable of probing the rapid conformational dynamics found in heterogeneous catalysts but has historically been restricted by its low sensitivity, limiting the detail with which structures can be resolved. Here, we apply solid-state NMR and dynamic nuclear polarization, in combination with density functional theory modeling, to reveal the high-resolution structure and motional freedom of a scandium supported complex in three dimensions. The results are contrasted with the study of the analogous homoleptic complex in the crystalline state, highlighting the impacts that surface structure may have on the dynamics of supported complexes.

Graphical Abstract

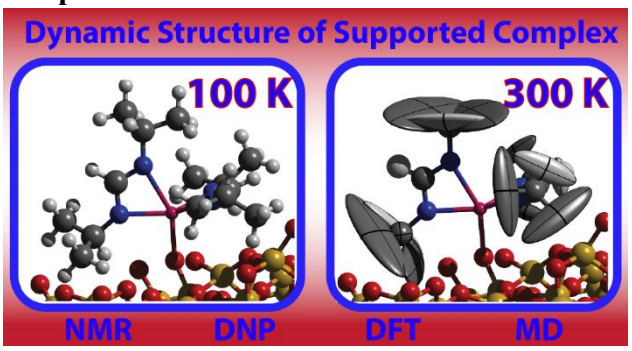

1. Introduction

It is well known that the structure of a metal catalyst is intimately related to its activity and selectivity. In fact, a number of numerical and graphical structural descriptors have been designed to relate the catalytic activity and selectivity of catalysts to the local structure of their active sites. Among them is the Tolman cone angle,[1] the accessible molecular surface,[2] the percentage of buried volume,[3-7] the sterimol steric parameters,[8] stereocartography,[9] solid angles,[10,11] and steric maps.[12-15] Generally, steric interactions are assumed to disfavor particular transition states and promote selectivity, for instance in the case of asymmetric catalysis.[16]

While the influence that molecular structure has on catalysis is well documented, static structures do not tell the whole story. Enzymes generally are highly dynamic and alter their structures through the principles of allostery and induced fit[17] to favor a given transition state and product.[18-20] The behavior of a catalytic site thus goes beyond so-called steric and electronic effects of a single structure, and it is necessary to consider the potential influence of structural dynamics on its performance. Note that while the term dynamics is often used in the context of catalysis to refer to bulk structural changes occurring over large timescales, such as particle migration, oxidation, etc.,[21] here it will be used exclusively in the context of molecular dynamics, namely, the conformational changes that occur at equilibrium that are responsible for the (de)stabilization of transition states.

Dynamics have been shown to influence not only enzyme chemistry but also homogeneous catalysis where structural flexibility has been linked to enhanced activity.[22-30] Similar arguments have also been made in the case of single-site heterogeneous catalysts.[31] In supported metal catalysis, the rapid dynamics of metal clusters has also been shown to generate short-lived highly-active species that are thought to dominate catalysis.[32,33] While the influence of dynamics have been noted, our understanding of their scope in most systems remains limited. To date, studies of dynamics have been largely limited to the realm of computation. Experimentally, few techniques are sensitive to motions occurring on the sub-nanosecond timescale, particularly those that do not lead to bulk structural changes. Chief among them is solid-state nuclear magnetic resonance (SSNMR) spectroscopy.

SSNMR spectroscopy has the potential to reveal not only the precise structure of a heterogeneous catalyst in three-dimensions, a feat that was recently demonstrated[34] with the use of sensitivity enhancement through dynamic nuclear polarization (DNP),[35-37] but also to reveal structural dynamics with the same level of detail. SSNMR measurements are site-specific, meaning that the motions throughout a molecule, or ligand, can be determined independently and their relationships can be used to elucidate the three-dimensional conformation space of a catalyst. This potential has already been demonstrated with the SSNMR observation of dynamic ligand exchange[38-41] as well as the observation that the metal dynamics in silica-supported Mo, Ta, W, and Re alkylidene catalysts may be related to the identity of the metal, with the lighter Mo catalysts being bound more tightly to the surface.[42] There is also SSNMR evidence that the “roughness” of the silica surface may prevent certain motional modes in surface-supported moieties.[43]

Herein we apply SSNMR spectroscopy to study the structure and dynamics of scandium amidinate species, as a homoleptic tris-ligand complex and its congener grafted to the surface of

silica. Rare earth amidinate complexes, including scandium complexes, are known to be efficient polymerization catalysts, and also have notable catalytic activity in reactions such as carbodiimide additions.[44] Both conventional and DNP-enhanced SSNMR spectroscopy, along with periodic density functional theory (DFT) simulations, are used to elucidate the podality and configuration of the supported complex and determine its static three-dimensional structure. We then use the ^{45}Sc SSNMR lineshape as well as site-specific ^{1}H-^{13}C and ^{1}H-^{45}Sc dipolar couplings to probe the conformational freedom of the complex. In combining these measurements with DFT-based molecular dynamics (MD) simulations we mapped the motions onto in space and obtain a dynamic three-dimensional structure for the supported metal complex.

2. Experimental

2.1. Synthesis

All manipulations were carried out under inert conditions, either using Schlenk techniques or in a glovebox under a purified nitrogen atmosphere, unless stated otherwise. Dry and degassed solvents were used throughout. Pentane was sparged with nitrogen, passed through activated alumina columns, and stored under nitrogen. Benzene-d_6 was degassed via three consecutive freeze-pump-thaw cycles, dried over Na/K alloy, vacuum transferred, and stored over molecular sieves under nitrogen. Tris(N,N'-di-*i*-propylformamidinato)scandium(III) was purchased from Strem Chemicals and used without further purification. Fumed silica (Aerosil) of surface area 300 m^2/g was purchased from Evonik, calcined at 300°C for 12 h and then partially dehydroxylated at 300 °C for 12 h. Titration of the surface silanols in this material with $Mg(CH_2Ph)_2(O_2C_4H_8)_2$ revealed a surface OH loading of 0.95 ± 0.05 mmol/g.

In a nitrogen glovebox, Sc(*i*PrNCHN*i*Pr)$_3$ (0.3 g, 0.70 mmol) was dissolved in anhydrous pentane (7 mL). This solution was added to a suspension of Aerosil (0.60 g) in pentane (7 mL), and the resulting mixture was stirred at room temperature for 4 h. The suspension was allowed to settle, and the supernatant liquid was decanted. The residual solid was washed with pentane (3 × 5 mL) and dried overnight *in vacuo* to afford a white powder. IR (DRIFTs, cm^{-1}): 3671, 3201, 2965, 2931, 2868, 2850, 2768, 2599, 1660 (C=N), 1558, 1464, 1377, 1359, 1341, 1320 (see Figure S8). Elemental analysis for Sc(*i*PrNCHN*i*Pr)$_2$@SiO_2: C, 8.45; H, 1.56; N, 2.61; Sc, 1.93.

The number of *i*PrNCHN*i*Pr groups per Sc center was determined using a combination of solution-state NMR experiments. We first performed titration experiment wherein methanol is used to protonate, and dissociate, the amidinate ligands that are bound to scandium. In an NMR tube containing a suspension of grafted Sc material (10.6 mg) in benzene-d_6, dry and degassed methanol (20 µL, 0.494 mmol) was added. The amount of free ligand was quantified by ^{1}H NMR to be 0.008 mmol, using tetrakis(trimethylsilyl)silane (5.3 mg, 0.016 mmol) as an internal standard. When combined with an ICP-OES measurement of the Sc loading (1.9 wt % Sc, 0.43 mmol Sc/g) this experiment revealed that there were 1.8 ± 0.2 *i*PrNCHN*i*Pr groups per Sc center. The grafting reaction was then repeated in an NMR tube to instead measure the quantity of amidinate ligands that are released during grafting. For this, Sc(*i*PrNCHN*i*Pr)$_3$ (14.2 mg, 0.0333 mmol) was dissolved in benzene-d_6 and added to a suspension of Aerosil (11.7 mg, 0.011 mmol Si-OH) in benzene-d_6 in the NMR tube. The amount of free ligand released during grafting was quantified by ^{1}H NMR to be 0.009 mmol, while there remained 0.0248 mmol of the free metal complex in

solution. As such, 0.0085 mmol of the complexes were consumed, releasing on average 1.06 free ligands each. 79% of all Si-OH sites on the surface were consumed. Hexamethylbenzene (2.8 mg, 0.017 mmol) was used as an internal standard.

2.2. Characterization Methods

Diffuse reflectance infrared Fourier transform (DRIFT) spectra were recorded on a Bruker VERTEX 80 IR spectrometer using a Harrick Praying Mantis accessory and a sealed, ambient-pressure sample chamber consisting of a dome with ZnSe windows. Elemental analysis was performed using a Perkin-Elmer 2400 Series II CHN/S. Inductively Coupled Plasma-Optical Emission Spectroscopy (ICP-OES) was performed to measure the amount of scandium present in the material. The samples (2.0 – 4.0 mg each) were digested for 24 h in aqueous HF and aqua-regia (0.18% and 5% respectively) and analyzed in a Perkin Elmer Optima 2100 DV Inductively Coupled Plasma-Optical Emission Spectroscope.

2.3. Solid-State NMR Spectroscopy

Conventional solid-state NMR experiments were performed using either an Agilent DD2 400 MHz spectrometer equipped with a 3.2 mm magic angle spinning (MAS) probe or a Varian VNMRS 600 MHz spectrometer equipped with either a 3.2 mm or a 1.6 mm MAS probe. All rotors were packed under an inert atmosphere using a glovebox and spun using nitrogen gas to limit air exposure. Room temperature $^{13}C\{^{1}H\}$ windowed proton-detected local field (wPDLF)[45,46] experiments were acquired at 9.4 T using a spinning frequency of 11.111 kHz and a 100 kHz ^{1}H radiofrequency (rf) power for all pulses. The ^{13}C inversion pulse lasted 5 μs. Heteronuclear dipolar recoupling was achieved using the $R18^5_2$ pulse sequence[47] and a $\pi/2_0–\tau–\pi/2_0$ composite *R* element with a 50% window duration.[48] Polarization transfer from ^{1}H to ^{13}C was achieved using cross-polarization with the contact time set to 150 μs to minimize ^{1}H spin diffusion and the intensity of the zero frequency spike. The t_1 evolution period was incremented in steps of 40 μs which consists of four composite inversion pulses, and the minimum step size for the experiment. A total of 32 t_1 increments were acquired, each consisting of 15,360 transients with a recycle delay of 1 s.

$^{1}H\{^{45}Sc\}$ rotational-echo saturation pulse double-resonance (RESPDOR)[49] experiments were performed using a spinning frequency of 33.333 kHz. ^{1}H excitation and refocusing pulses utilized a 100 kHz radiofrequency power and heteronuclear dipolar recoupling was achieved using the $SR4^2_1$ recoupling sequence[50,51] and a π_0 basic *R* element. The recoupling time was incremented in steps of 120 μs, consisting of 8 ^{1}H composite inversion pulses. 128 scans were accumulated for each t_1 increment with a recycle delay of 2 s.

^{1}H double-quantum single-quantum (DQ/SQ) experiments were performed using the back-to-back (BaBa) recoupling sequence[52] and recoupling was achieved using a total of two rotor cycles of recoupling for both excitation and reconversion. The spinning frequency was set to 36 kHz. A total of 64 t_1 increments of 27.78 μs were acquired, each consisting of 128 scans with a recycle delay of 1 s.

^{45}Sc SSNMR experiments were performed on either static or spinning samples with the spinning frequency set to 16 kHz for the latter. A Hahn echo pulse sequence was used with an echo delay of 62.5 μs for both the static and MAS experiments. Recycle delays were set to 1 s and scans

totaled between 1024 and 10240 for the molecular complex and 57,344 and 32,768 for the grafted complex in the experiments performed at 9.4 and 14.1 T, respectively.

DNP-enhanced solid-state NMR experiments were performed using a Bruker 400 MHz/264 GHz MAS-DNP NMR spectrometer equipped with a 3.2 mm low-temperature MAS probe.[53] To enable simultaneous tuning to both ^{13}C and ^{45}Sc (100.7 and 97.3 MHz, respectively) the X channel of the probe was split with the use a REDOR box manufactured by NMR-service. All DNP experiments were performed at around 100 K with samples impregnated with a 16 mM solution of the TEKPol biradical[54] in dry 1,1,2,2-tetrachloroethane;[55] in the case of the wPDLF experiment perdeuterated 1,1,2,2-tetrachloroethane was used.[56] The recycle delay was set to 4.7 s, which corresponded to 1.3 T_1, to maximize sensitivity. Polarization transfer from hyperpolarized ^{1}H spins was achieved with 650 μs of cross-polarization with the exception of the wPDLF experiments where it was reduced to 150 μs. ^{13}C{^{45}Sc} RESPDOR was performed at a spinning frequency of 10 kHz using XY-8[57] rotational-echo double-resonance (REDOR) recoupling.[58] The ^{13}C inversion pulses used for REDOR lasted 10 μs. The recoupling time was incremented in steps of 400 μs and each spectrum consisted of 320 scans. The split 1.5t_R ^{45}Sc saturation pulse[59] had a radiofrequency power of roughly 100 kHz which was sufficient to saturate the RESPDOR dephasing. The same sequence was used to recouple ^{15}N-^{45}Sc dipolar interactions, however, the ^{45}Sc saturation pulse no longer needed to be split as it was possible to apply simultaneous pulses to both ^{15}N and ^{45}Sc. The recoupling time was incremented in steps of 800 μs and a total of 128 scans were acquired for each spectrum. The ^{15}N inversion pulses lasted 12 μs and the contact time was set to 4 ms. DNP-enhanced ^{13}C{^{1}H} wPDLF experiments were performed using the same radiofrequency power and spinning frequency as those used for the room temperature measurements. 32 scans were acquired for each t_1 increment and the recycle delay was set to 4 s.

2.4. Density Functional Theory

Plane-wave DFT calculations were carried out using the CASTEP software package (version 2018).[60] NMR calculations were performed using the Gauge-Including Projector Augmented-Wave (GIPAW) module as implemented within CASTEP.[61,62] The exchange-correlation (XC) functional of Perdew, Burke, and Ernzerhof (PBE)[63] was used for all calculations with a plane-wave energy cutoff of 489.8 eV and reciprocal space sampled by the Γ point. Total energies were converged to changes below 2×10^{-6} eV/atom.

Geometry optimizations were carried out using the default "on-the-fly" ultrasoft pseudopotentials (USPP) contained within CASTEP.[64] Calculations on the molecular complex were conducted with the molecule suspended in a 50 Å × 50 Å × 50 Å box. The structure of the molecule was optimized with a maximum force tolerance of 5×10^{-2} eV/Å, a maximum atomic displacement tolerance of 2×10^{-3} Å, and a total energy convergence tolerance of 2×10^{-5} eV/atom.

To model the grafted molecule, multiple amorphous silica surfaces were used which were based on the models reported by Comas-Vives.[65] These structures were re-optimized to account for differences in XC functional, pseudopotentials, etc. Following this optimization, the scandium complex was attached to an appropriate hydroxyl site on the surface, replacing the H with the complex. The bottom six atomic layers of the silica surface were then fixed, and the other atomic positions were allowed to relax. The constraints on the geometry optimization were a maximum

force tolerance of 0.1 eV/Å, a maximum atomic displacement tolerance of 5×10^{-3} Å, and a total energy convergence tolerance of 5×10^{-5} eV/atom.

For GIPAW calculations of both the molecular complex and the grafted molecules, a custom Sc USPP was used. A known issue with magnetic shielding calculations of some alkaline earth and rare earth elements is that the amount of hybridization between the oxygen 2p and unoccupied d and f orbitals is overestimated.[66] This has affected calculated magnetic shielding constants in systems containing Ca^{2+}, Sc^{3+}, and La^{3+}, among others.[67,68] The spurious hybridization can be mitigated by shifting the appropriate d or f pseudopotential channel to a higher energy.[66] The details of how we selected an appropriate energy for shifting the Sc 3d orbital are provided in the supporting information.

The electric field gradient (EFG) and magnetic shielding tensors were calculated for all systems. Isotropic magnetic shielding constants (σ_{iso}) were converted to isotropic chemical shifts using the usual relation ($\delta_{iso} = \sigma_{ref} - \sigma_{iso}$). σ_{ref}, which in the case of ^{45}Sc corresponds to the ^{45}Sc magnetic shielding in a 0.06 M solution of $Sc(NO_3)_3$ in D_2O, was determined through the calculation of the shielding in a secondary solid reference compound: Sc_2O_3.[69] Sc_2O_3 contains two crystallographically inequivalent Sc sites for which we calculated σ_{iso} values of 770.41 ppm and 749.92 ppm. Using the experimental δ_{iso} values reported by Kim *et al*.,[70] we obtained a computed σ_{ref} value of 874.3 ppm.

In addition to calculating the NMR parameters of the static structures, calculations were also performed on randomly-selected snapshots of the MD calculation. Ten snapshots were used for the calculation of magnetic shielding tensors, while the EFG tensors were calculated for sixty snapshots.

2.5. Molecular Dynamics

MD simulations were performed using plane-wave DFT via the VASP package (version 5.4.4.).[71,72] We used the PBE exchange-correlation functional and the standard projector-augmented-wave (PAW) potentials that are included in the package.[73,74] The plane-wave energy cutoff was set to 400 eV. The NVT (or canonical) ensemble and the Nose-Hoover thermostat were used for temperature control.[75,76] In order to obtain sufficiently long trajectories for NMR analysis (up to 100 ps), the DFT optimized structures (section 2.4) were truncated with the following procedure. First, all silicon atoms that are separated from the scandium atom by a distance greater than a cutoff value L_c were discarded. The coordination spheres of the remaining silicon atoms were then completed, and the oxygen dangling bonds were capped by hydrogen atoms. All atoms that are left unconnected with the central cluster were discarded. Finally, we froze all silicon atoms that are farther than $L_c/2$ from the scandium center. To improve computational efficiency, the truncated system was also placed in a smaller box for the MD simulations than was used for the geometry optimization. For example, using L_c=9 Å, we reduce a system consisting of 103 Si atoms to a system of 23 Si atoms for MD simulations, in a 20 Å × 20 Å × 20 Å box. All simulations are conducted at a temperature of 300 K.

3. Theory

3.1. Dipolar Coupling

Nuclear spins couple with one another directly through dipolar coupling.[77] The dipolar coupling constant (R_{DD}) depends only on the internuclear distance ($r_{1,2}$) as well as some fundamental constants, namely the permittivity of free space (μ_0), the gyromagnetic ratios of the nuclei involved (γ_i), and the reduced Planck constant ($\hbar$).

$$R_{DD} = \left(\frac{\mu_0}{4\pi}\right)\left(\frac{\gamma_1\gamma_2\hbar}{2\pi}\right)r_{1,2}^{-3} \quad (1)$$

The interaction produces a splitting ($\Delta\nu_D$) of the lines that depends on the angle (θ) between the internuclear vector and the magnetic field, B_0.

$$\Delta\nu_D = R_{DD}(3\cos^2\theta - 1) \quad (2)$$

As a result of dynamic processes, θ becomes time-dependent and, as such, so does $\Delta\nu_D$. In the case of single-bond dipolar coupling, $r_{1,2}$, and as such R_{DD}, is generally assumed to be largely time-independent. This approximation is, however, invalid in the case of multiple bond coupling, in which case it is important to consider both the time dependence in θ as well as $r_{1,2}$. In this circumstance, it is most convenient to describe the interaction as a Cartesian tensor, **D**. **D** is a traceless and axially-symmetric tensor (at least in the absence of dynamics) that is given by the following in its principal axis system (PAS), i.e., with the internuclear vector oriented along the magnetic field.

$$\mathbf{D}_{PAS} = R_{DD}\begin{bmatrix}1 & 0 & 0\\ 0 & 1 & 0\\ 0 & 0 & -2\end{bmatrix} \quad (3)$$

The orientation of the internuclear vector with respect to the magnetic field can be described using a polar angle system (ϕ and θ) where ϕ is the positive angle between the projection of the internuclear vector in the plane perpendicular to B_0 and an arbitrary vector within this plane designated as the x axis. We used the procedure described by Bryce et al.[78] to calculate θ and ϕ from a molecular structure. The Cartesian tensor can be rotated away from its PAS to the direction of the internuclear vector (the LAB frame) as follows:

$$\mathbf{D}_{LAB} = \mathbf{R}^{-1}(\theta,\phi)\mathbf{D}_{PAS}\mathbf{R}(\theta,\phi) \quad (4)$$

where the rotation matrix **R** is given by:

$$\mathbf{R}(\theta,\phi) = \begin{bmatrix}\cos\theta\cos\phi & \cos\theta\sin\phi & -\sin\theta\\ -\sin\phi & \cos\phi & 0\\ \sin\theta\cos\phi & \sin\theta\sin\phi & \cos\theta\end{bmatrix} \quad (5)$$

In this new coordinate system, the dipolar coupling tensor takes the form:

$$\mathbf{D}_{LAB} = R_{DD}\begin{bmatrix}\cos^2\phi(1-3\sin^2\theta)+\sin^2\phi & 3/2\sin2\phi\sin^2\theta & 3\cos\theta\cos\phi\sin\theta\\ 3/2\sin2\phi\sin^2\theta & \cos^2\phi+\cos^2\theta\sin^2\phi-2\sin^2\theta\sin^2\phi & -3\cos\theta\sin\phi\sin\theta\\ 3\cos\theta\cos\phi\sin\theta & -3\cos\theta\sin\phi\sin\theta & 1-3\cos^2\theta\end{bmatrix}. \quad (6)$$

In the fast motion limit it is sufficient to describe a new motionally-averaged dipolar coupling tensor, $\mathbf{D}_{ave}$, which is simply the element-wise average of $\mathbf{D}_{LAB}$.

$$\mathbf{D}_{\text{ave}} = \frac{1}{t}\int_0^t \mathbf{D}_{\text{LAB}} dt \quad (7)$$

We can then diagonalize $\mathbf{D}_{\text{ave}}$ to extract its three new principle components ($|D_{11}| \leq |D_{22}| \leq |D_{33}|$). The averaged dipolar coupling constant $\langle R_{\text{DD}} \rangle$ is given by -D_{33}/2. Dynamics may also introduce a non-zero dipolar asymmetry ($\eta_{\text{D}} = \frac{D_{11} - D_{22}}{D_{33}}$); however, this asymmetry seldom impacts the results of dipolar coupling experiments such as those performed as a part of this study. As such it is possible to summarize the experimental impact of the dynamic motions into a single parameter known as the order parameter, $\langle S \rangle$, which simply corresponds to the factor by which the magnitude of the dipolar coupling is reduced by the dynamic motions.

$$\langle S \rangle = \frac{\langle R_{\text{DD}} \rangle}{R_{DD}} \quad (8)$$

Innumerable different motional modes can produce the same value of $\langle S \rangle$, however, in increasing the number of $\langle S \rangle$ values that are measured for a given molecule or site it is possible to rule out certain scenarios. Usually some form of full[79] or hindered[43,80,81] rotation about a particular axis, such as a Gaussian oscillation or the typical methyl rotation, is invoked, however, we will instead be coupling SSNMR measurements with the molecular dynamics calculations of $\langle S \rangle$.

3.2. Second-Order Quadrupolar Coupling

The approach outlined in section 3.1 is only valid in the limit of fast dynamics and for first-order properties such as dipolar coupling, first-order quadrupolar coupling, and chemical shift anisotropy. When the dynamics appear on the NMR timescale, or involve a second-order property, such as the second-order quadrupolar effects that influence the central transition (m = ½ to -½) of a half-integer quadrupolar nucleus (spin $I > 1$), a different approach is required. This section will revise how the impacts of dynamics on the NMR spectra of a half-integer quadrupolar nucleus (^{45}Sc, $I = 7/2$) can be modeled.

The shift in the resonance frequency of the central transition of a quadrupolar nucleus, ignoring chemical shift effects, is given by the following expression where the quadrupolar coupling constant can be obtained through its usual definition ($C_{\text{Q}} = \frac{eQV_{33}}{h}$).[82]

$$\omega_{\text{CT}} = \left[\frac{eQ}{4I(2I-1)\hbar}\right]^2 \frac{6[4I(I+1)-3]}{\omega_0}[2V_1V_{-1} + V_2V_{-2}] \quad (9)$$

The second-rank quadrupolar spherical tensor in its PAS is given as the following.

$$\mathbf{V}_{\text{PAS}} = \begin{bmatrix} V_{-2,\text{PAS}} \\ V_{-1,\text{PAS}} \\ V_{0,\text{PAS}} \\ V_{1,\text{PAS}} \\ V_{2,\text{PAS}} \end{bmatrix} = \begin{bmatrix} \eta V_{33}/\sqrt{24} \\ 0 \\ V_{33}/2 \\ 0 \\ \eta V_{33}/\sqrt{24} \end{bmatrix} \quad (10)$$

The quadrupolar asymmetry parameter, η, is defined as $\eta = \frac{V_{11} - V_{22}}{V_{33}}$ and the EFG tensor principal components, V_{ii}, are ordered as $|V_{11}| \leq |V_{22}| \leq |V_{33}|$.

The values of V_i in the lab frame can be calculated with a sequence of Wigner rotations, for instance as[83]

$$\mathbf{V}_{\mathrm{LAB}} = \boldsymbol{\mathcal{D}}^2(\phi,\theta,0)\boldsymbol{\mathcal{D}}^2(\alpha_i,\beta_i,\gamma_i)\mathbf{V}_{\mathrm{PAS}} \quad (11)$$

for the calculation of the resonance frequency in the static case, where α_i, β_i, and γ_i are the Euler angles relating the molecular orientation 'i' to the crystal frame, and

$$\mathbf{V}_{\mathrm{LAB}} = \boldsymbol{\mathcal{D}}^2(\omega_R t + \gamma_{\mathrm{rot}},\theta_M,0)\boldsymbol{\mathcal{D}}^2(\phi,\theta,0)\boldsymbol{\mathcal{D}}^2(\alpha_i,\beta_i,\gamma_i)\mathbf{V}_{\mathrm{PAS}} \quad (12)$$

when including MAS,[84] where θ_M is the magic angle ($\theta_M = \cos^{-1}\sqrt{1/3} \approx 54.74°$), ω_R is the spinning frequency in angular units, t is time, and γ_{rot} is the rotor phase at time zero. $\boldsymbol{\mathcal{D}}^2$ are second-rank Wigner rotation matrices that have elements of

$$\mathcal{D}^2_{m,n}(\alpha,\beta,\gamma) = e^{-im\alpha} d^2_{m,n}(\beta) e^{-in\gamma} \quad (13)$$

where $d^2_{m,n}(\beta)$ are the reduced Wigner rotation matrix elements.

To calculate the effects of intermediate dynamics on the lineshape calculations must be performed in the time domain. The free induction decay $G(t)$ is calculated by propagating the transverse magnetization $M(t)$ according to the instantaneous resonance frequency, which is calculated using equation 9. Note that here $M(t)$ and $G(t)$ are equivalent.

$$G(t) = M(t) = \exp\left[i\omega_{\mathrm{CT}} t\right] M(0) \quad (14)$$

In the case of MAS, the resonance frequency becomes time-dependent and as such small time steps Δt need to be used during which $\omega_{\mathrm{CT}}(t)$ can be assumed to be time independent.

$$G(t) = M(t) = \exp\left[i\omega_{\mathrm{CT}}(t)\Delta t\right] M(t - \Delta t) \quad (15)$$

Jump dynamics can be included in equations 14 and 15 using an exchange matrix **K** with off-diagonal elements of $k_{i,j}$, the exchange rate constant for a jump between orientations i and j, and diagonal elements of:

$$k_{i,i} = \sum_{j,j \neq i} - k_{i,j}. \quad (16)$$

The rate constants $k_{i,j}$ are related to the free energy of activation of the motion ($\Delta G^{\ddagger}_{i,j}$) through the following relationship where k_B is the Boltzmann constant, T is the temperature, and R is the gas constant.

$$k_{i,j} = \frac{k_B T}{h} \exp\left(\frac{-\Delta G^{\ddagger}_{i,j}}{RT}\right) \quad (17)$$

The resonance frequencies of the different jump orientations are organized into a diagonal matrix **Ω** with elements of $\omega_{\mathrm{CT},i}(t)$ to reformulate equation 15 as:

$$\mathbf{M}(t) = \exp\left[\left[i\boldsymbol{\Omega} + \mathbf{K}\right]\Delta t\right] \mathbf{M}(t - \Delta t) \quad (18)$$

There, $\mathbf{M}(t)$ is a column vector with elements, $M_i(t)$, corresponding to the magnetization associated with each jump orientation i; at time zero, $M_i(0) = 1$. The free induction decay signal is simply the sum of the magnetization from each of these jump orientations.

$$G(t) = \sum_i M_i(t) \quad (19)$$

The NMR spectrum is then obtained by performing a Fourier transformation of the free induction decay signal $G(t)$. Powder averaging was accomplished by looping over θ from 0 to π in a cosinusoidal fashion, to produce the correct $\sin\theta$ statistical distribution, and ϕ and γ_{rot} were looped from 0 to 2π linearly.

4. Results and Discussion

4.1. Molecular Complex

A schematic representation of the structure of the tris(N,N'-di-*i*-propylformamidinato)scandium(III) complex (**1**) is given in Figure 1b. This complex features three bidentate amidinate ligands that bond to a six-coordinate Sc forming three metallocyclic 4-membered rings; the N-bonded substituents on the amidinates are *i*-propyl groups (*i*Pr). The high rigidity of the amidinate chelate ring allows the motion of the central carbon and hydrogen atoms on the ligand to be used to directly probe the motions of the Sc center, for instance, free rotation about the Sc-O bond in the grafted analogue. The *i*Pr groups can undergo two additional rotations, about the N-C bond and about the C-C bond, giving methyl rotation, both of which can be probed through the measurement of ^{1}H-^{13}C dipolar coupling (see section 3.1.).

We first performed a ^{13}C{^{1}H} wPDLF experiment on this sample. The wPDLF sequence used in this study is depicted in Figure 1a. The ^{1}H-^{13}C dipolar interactions are first recoupled using the γ-encoded $R18_2^5$ pulse sequence[47] employing a windowed *R* element[48] which serves to greatly improve the robustness of the sequence with respect to rf maladjustments.[46,85] The phase of the recoupling is then inverted to refocus the recoupled ^{1}H CSA while the refocusing of the ^{1}H-^{13}C dipolar interaction is prevented by the simultaneous application of a ^{13}C inversion pulse. A short cross-polarization (CP) contact time is then applied to transfer the dipolar-modulated ^{1}H magnetization to its directly-bonded ^{13}C site for detection. γ-encoded sequences produce much more pronounced dipolar oscillations than their non-γ-encoded counterparts and can be Fourier transformed to obtain a well-resolved doublet for each ^{1}H-^{13}C spin pair. Like sequences such as polarization inversion spin exchange at the magic angle (PISEMA),[86] this potentially enables for the distinction of multiple overlapping order parameters from the same resonance, for instance in the event that the dynamics are non-homogeneous. This cannot be done with sequences such as dipolar chemical shift correlation (DIPSHIFT)[87] and REDOR.[58] Since the dipolar interactions are reintroduced onto the ^{1}H magnetization, the behavior is identical for CH, CH_2 and CH_3 moieties in the absence of dynamics, which further simplifies the analysis.[45]

The ^{13}C{^{1}H} CPMAS and wPDLF spectra acquired on **1** are shown in Figure 1b. In the wPDLF spectrum dashed horizontal lines highlight the expected dipolar splitting for a rigid C-H bond. Clearly, all the dipolar couplings are dramatically reduced with the amidinate carbon 'A' having an $\langle S \rangle$ of 0.12, with the other carbon sites featuring further smaller $\langle S \rangle$ values. This indicates that the complex undergoes nearly isotropic motions in the crystal. The DFT-optimized structure

for this complex does have a somewhat round shape and thus these motions are understandable (Figure S7).

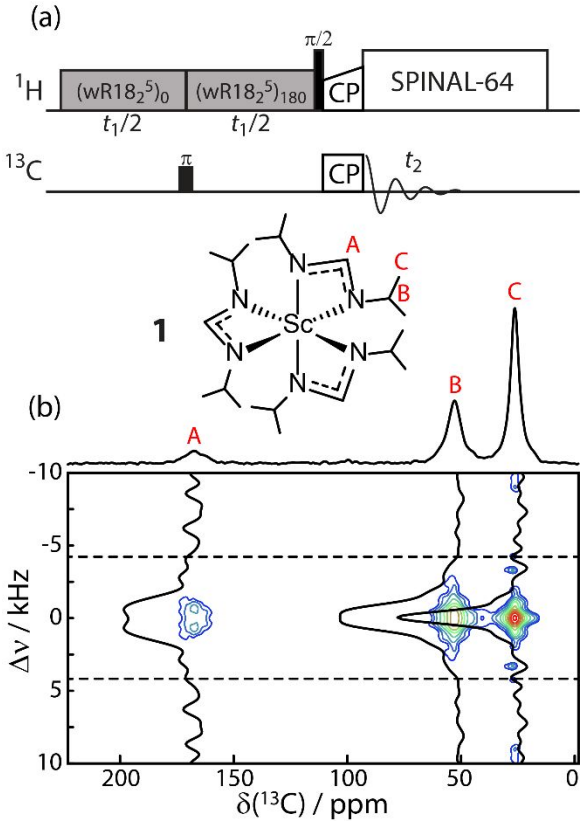

Figure 1. (a) ^{13}C{^{1}H} wPDLF pulse sequence diagram. (b) 2D ^{13}C{^{1}H} wPDLF NMR spectrum of the molecular Sc complex **1**. The structure of the complex is depicted above the spectrum with its three chemically-distinct ^{13}C sites labelled on both the structure and the spectrum. The ^{13}C{^{1}H} CPMAS NMR spectrum is overlaid above the 2D wPDLF spectrum and slices along the dipolar coupling dimension are shown to display the recoupled dipolar doublets. Dashed lines in (b) highlight the expected dipolar splitting in the absence of C-H dynamics.

To corroborate these measurements, we additionally measured the ^{1}H-^{45}Sc dipolar couplings using a ^{1}H{^{45}Sc} RESPDOR experiment (Figure 2a). SR4$^2_1$ dipolar recoupling[50] was applied at the ^{1}H frequency to simultaneously recouple ^{1}H-^{45}Sc dipolar interactions and decouple the ^{1}H homonuclear dipolar interactions. Two datasets are acquired both in the presence or absence of a ^{45}Sc saturation pulse which produces a reference dataset (S_0) and a recoupled dataset (S). The normalized difference between the two ($\Delta S/S_0$) can be simulated with existing analytical expressions.[51] A dephasing efficiency of 75% was assumed for all RESPDOR simulations throughout this study.

As can be seen from the experimental RESPDOR dephasing curve for ^{1}H 'A' in **1** (Figure 2c), the dephasing is far slower than would be expected from a rigid ^{1}H-^{45}Sc internuclear vector and is best fitted with an order parameter of 0.2, in agreement with the ^{13}C{^{1}H} wPDLF result.

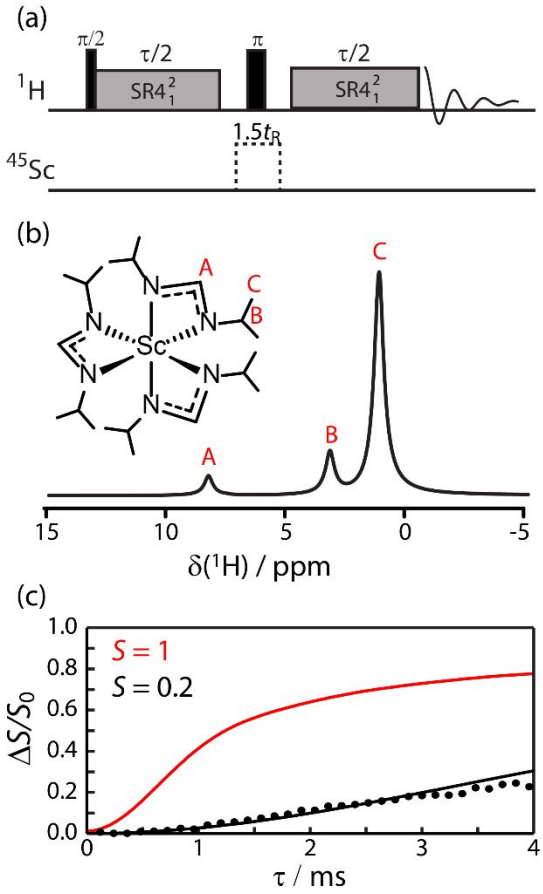

Figure 2. (a) ^{1}H{^{45}Sc} RESPDOR pulse sequence diagram. A dashed pulse on the ^{45}Sc channel indicates that this pulse is either applied or ignored to acquire the S and S_0 signals, respectively. (b) ^{1}H MAS NMR spectrum of molecular Sc complex **1**. The different ^{1}H resonances are labeled both on the spectrum and the molecular structure depicted above it. (c) ^{1}H{^{45}Sc} RESPDOR dephasing curve measured for ^{1}H site A. Two simulated curves are shown corresponding to H-Sc order parameters of 1 (red) and 0.2 (black) demonstrating that the Sc-H vector is dynamic.

To gain further information into the type of motion the complex undergoes in the crystal we have analyzed the ^{45}Sc static and MAS NMR lineshapes (see Figure 3). As the second-order quadrupolar interaction felt by the central transition of a quadrupolar nucleus requires icosahedral symmetry to average, rather than cubic symmetry in the case of the dipolar interaction, it is able to probe a wider range of motions.[83] The static lineshapes at room temperature resemble those expected from CSA, an interaction which would be eliminated by MAS. The MAS spectra, however, also resemble CSA powder patterns, albeit with an inverted skew. The only dynamic mode we were able to identify that could simultaneously replicate both the static and MAS lineshapes was one where the complex reorients itself in the crystal along the vertices of a cube; for instance with α = {0, 90°, 180°, 270°}, β = 54.74°, and γ = 0° (see Figure 3). This dynamic mode is also in agreement with the minute ^{1}H-^{13}C order parameters measured for this complex as this type of motions would completely average the ^{1}H-^{13}C and ^{1}H-^{45}Sc dipolar interactions (i.e., $\langle S \rangle = 0$).

We have further acquired the ^{45}Sc MAS spectra as a function of temperature from 300 to 100 K in order to determine the timescale of the reorientation. The data around the coalescence point (~250 K) are shown in Figure 3a; no significant lineshape changes occurred outside of this range. All spectra were fit to a single $\Delta G^{\ddagger}$ value of 48 ± 1 kJ/mol, with the exchange constant for a given temperature calculated according to equation 17. The next section will evaluate how the dynamics of this complex are impacted by its anchoring onto a solid surface.

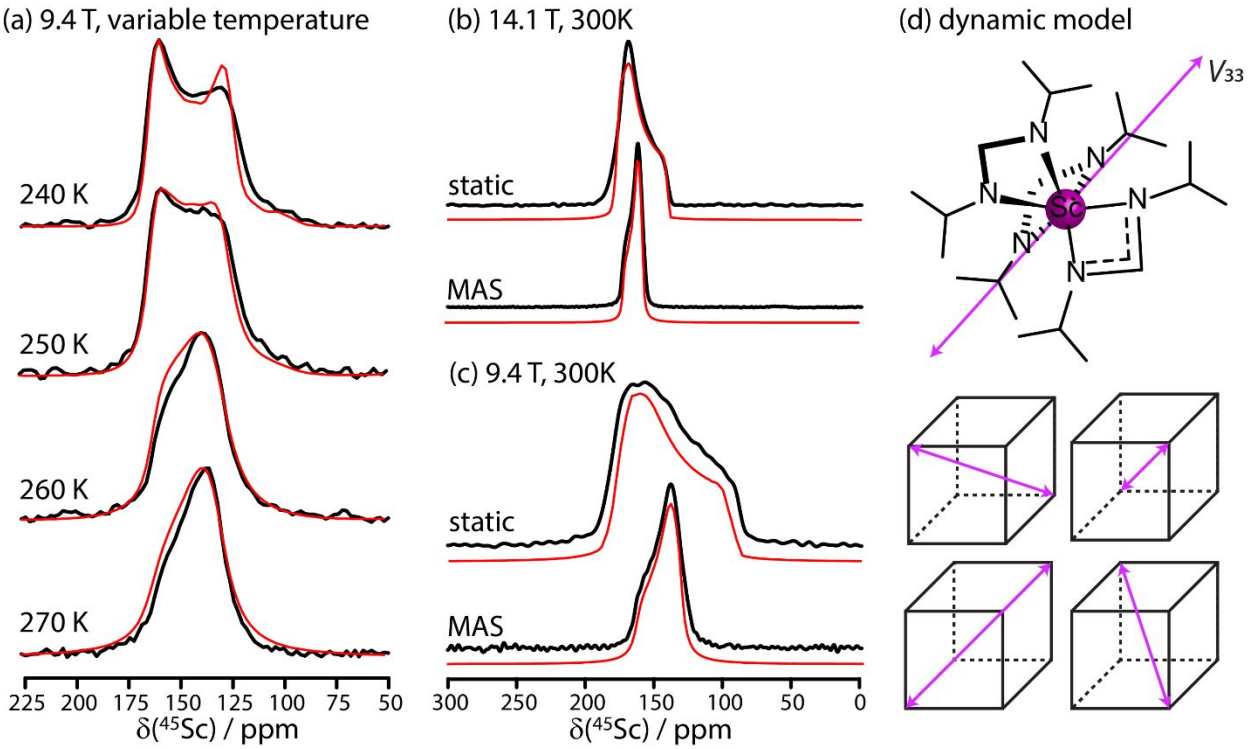

Figure 3. (a) ^{45}Sc MAS spectra acquired at a magnetic field of 9.4 T and the indicated temperature (black) with simulations (black) using a $\Delta G^{\ddagger}$ value of 48 kJ/mol for the reorientation. Static and MAS spectra acquired at two fields of 14.1 T (b) and 9.4 T (c) are also shown which were acquired at 300 K. Simulations were performed using the fourfold jump model depicted in (d). This corresponds to tetrahedral/cubic rearrangement of the V_{33} EFG tensor component (pink double arrow) which is aligned perpendicular to the plane encompassing the three amidinate ligands.

4.2. Grafted Complex

4.2.1. Configuration and Podality

Grafting **1** onto the surface of silica can produce a number of different configurations, the four most likely being depicted in Figure 4. Generally, the formation of a Sc-O bond with the silica requires the protonation of an amidinate ligand by the surface silanol, which results in the dissociation of the resulting amidine molecule. In principle, mono- (**3**) di- (**2**) and tripodal complexes can be formed, however the complex is unlikely to find the three nearby silanols required to form a tripodal complex. In addition, dipodal complexes featuring protonated ligands (**4** and **5**) may also be formed if the ligand remains coordinated to the scandium center after the complex is grafted.

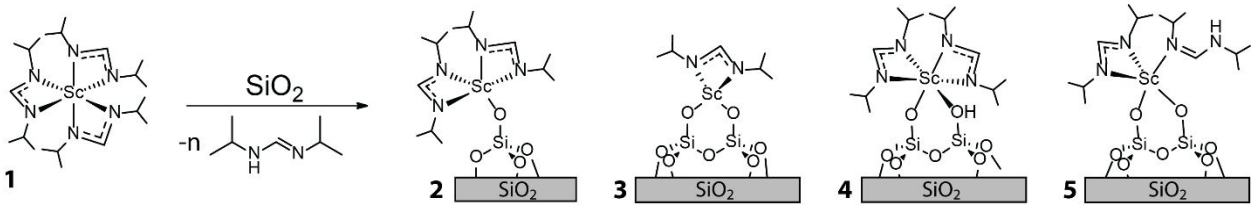

Figure 4. Scheme depicting the grafting reaction of **1** with silica. Four possible coordination modes are listed (**2-5**).

We first performed ^{1}H-^{1}H double-quantum-single-quantum (DQ/SQ) spectroscopy, using the BaBa sequence,[52] on the grafted complex in order to determine whether dipodal complex **3** is the dominant configuration. This complex has only a single 'A' proton (see Figures 4 and 5) and as such cannot form an A-A double-quantum coherence. As can be seen in Figure 5, the dominant correlation to ^{1}H 'A' was to another 'A' site from an adjacent ligand, strongly suggesting that there are two ligands coordinated to the metal, although there is a distinct possibility of having inter-complex correlations.

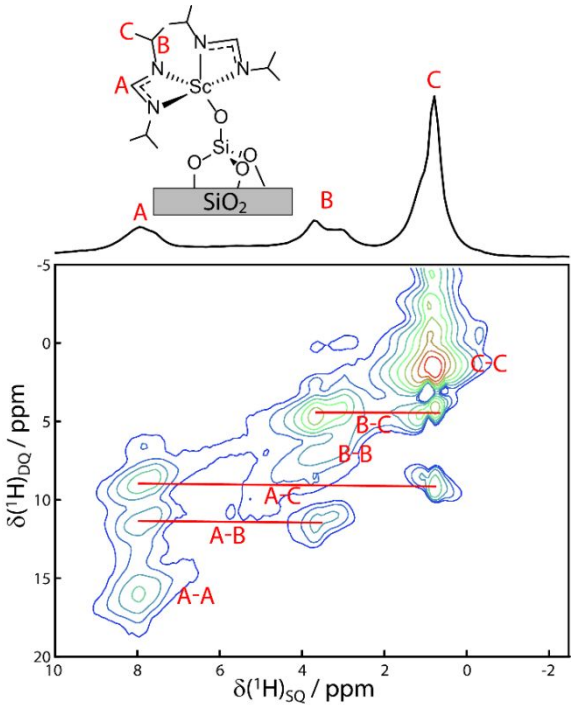

Figure 5. 1D ^{1}H MAS and 2D ^{1}H-^{1}H DQ/SQ NMR spectra of the grafted complex. The peaks and their assignments are labeled onto structure **2**. Correlations between all three sites are observed, including a dominant homocorrelation for site A, demonstrating that there are multiple amidinate ligands coordinated to the Sc center. A shoulder next to the resonance from site C may be due to free silanols.

We next acquired the ^{45}Sc MAS NMR spectra for this complex, which featured a lineshape broadened by a distribution of EFG tensor parameters (see Figure 6). Its simulation using a Gaussian distribution of C_Q values and a flat distribution of η values, using the software quadfit,[88] suggested that the mean C_Q is of 17 MHz and has a standard deviation of 4 MHz, and that the mean

isotropic chemical shift is 125 ppm (see Table 1). To analyze the data we performed GIPAW DFT calculations of the ^{45}Sc EFG and magnetic shielding tensors for compounds **1**–**4** (**5** was ignored as it does not agree with ^{13}C/^{15}N{^{45}Sc} RESPDOR measurements, *vide infra*). Three to five grafting locations onto previously-published amorphous silica structures[65] were trialed to evaluate the variability of the parameters. In addition, for one of these grafting locations the GIPAW DFT calculations were repeated for various snapshots of an MD simulation to view to what degree the parameters vary for a given single grafting location. The ^{45}Sc EFG and magnetic shielding tensors were found to vary considerably for all grafted structures, in agreement with the experimental spectra (see Table 1), however, the four-coordinate structure **3** had far larger predicted C_Q values than those measured experimentally and thus, in agreement with the ^{1}H DQ/SQ data, it is unlikely to exist in large quantities on the surface. This result is also in agreement with our methanol titration experiments that showed that there are 1.8 ± 0.2 amidinate ligands for every grafted Sc atom, as well as our *in situ* grafting reaction that showed that 1.06 amidines is released for each complex that gets grafted to the surface. In addition, from elemental analysis we measured that there are 2.2 ± 0.3 ligands per Sc. Similar analyses have been done in the past to study the coordination of grafted Sc complexes.[89,90]

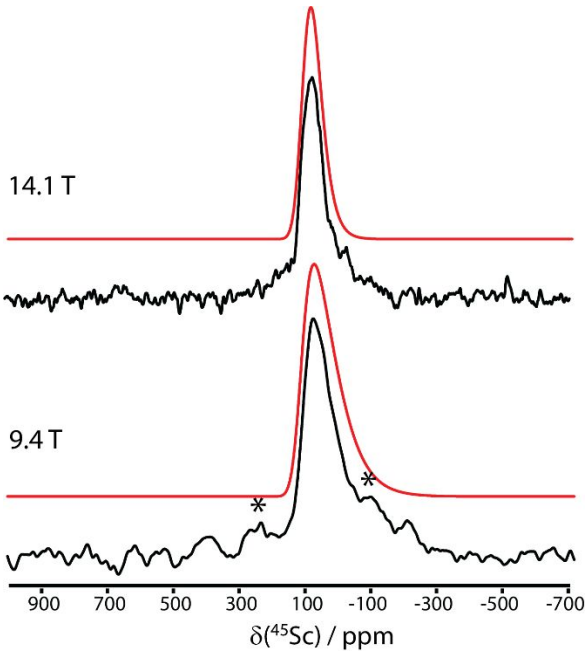

Figure 6. ^{45}Sc MAS NMR spectra of the grafted complex acquired at magnetic fields of 14.1 T (top) and 9.4 T (bottom). Best fit simulated spectra are overlaid in red.

Table 1. Experimental and DFT-calculated ^{45}Sc NMR parameters.

sample	δ_{iso} / ppm[a]	$s_n(\delta_{iso})$[b] / ppm	$\lvert C_Q\rvert$ / MHz[c]	$s_n(\lvert C_Q\rvert)$[b] / MHz	η	$s_n(\eta)$[b]
1, expt	177 ± 2	0	11.0 ± 0.3	0.0	0.1 ± 0.1	0.00
1, calc.	167	0	8.1	0.0	0.57	0.00
2, expt.	125 ± 15	20	17.0 ± 3.0	4.0	0.50	□[d]
2, calc.[e]	186	24	33.6	8.3	0.46	0.21
2, calc.[f]	201	13	22.9	6.3	0.60	0.23

3, calc.[g]	241	8	43.2	6.0	0.78	0.16
4, calc.[h]	135	3	23.1	1.3	0.34	0.04

[a]Calculated δ_{iso} values were obtained using an absolute shielding constant (σ_{ref}) of 874.26 ppm, which was calculated using Sc_2O_3. [b]In simulations and calculations involving ranges of parameters the average and standard deviation (s_n) for the range are given. [c]Calculated C_Q values were obtained using a nuclear quadrupole moment of -220 mb.[91] [d]All η values were given equal probability. [e]The values correspond to the average and standard deviation of the ^{45}Sc NMR parameters calculated for **2** when considering 5 different grafting locations. [f]The values correspond to the average and standard deviation of the ^{45}Sc NMR parameters calculated for 10 MD snapshots (δ_{iso}) and 60 MD snapshots ($|C_Q|$) of the same structure for **2**. [g]The values correspond to the average and standard deviation of the ^{45}Sc NMR parameters calculated for **3** when considering 3 different grafting locations. [h]The values correspond to the average, and standard deviation, of the ^{45}Sc NMR parameters calculated for **4** when considering 3 different grafting locations. Non-averaged values are reported in the supporting information.

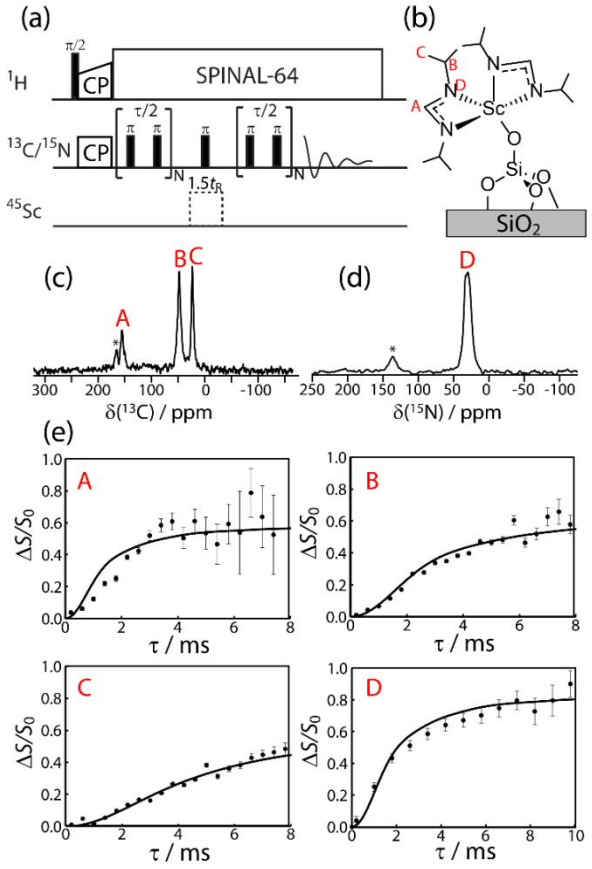

Figure 7. (a) ^{13}C/^{15}N{^{45}Sc} RESPDOR pulse sequence. Note that REDOR recoupling is used with an XY-8 phase cycle. A dashed pulse on the ^{45}Sc channel indicates that this pulse is either applied or ignored to acquire the S and S_0 signals, respectively; in the case of ^{13}C the ^{45}Sc pulse was split into two $0.75t_R$ pulses since simultaneous pulsing at the ^{13}C and ^{45}Sc channels was not possible. The structure for the grafted complex **2** is shown in (b) with the ^{13}C and ^{15}N sites labeled according to the ^{13}C{^{1}H} and ^{15}N{^{1}H} CPMAS NMR spectra in (c) and (d), respectively. There, an asterisk

is used to denote the resonance from a partial degradation product. $^{13}C/^{15}N\{^{45}Sc\}$ RESPDOR dephasing curves are shown in (e) for the four sites along with the simulated dephasing curves calculated using the DFT-optimized structure of **2**, demonstrating the good agreement with this structure. Error bars in (e) correspond to the inverse of the signal-to-noise ratios.

The DFT-optimized structures discussed above can also be directly compared to experiment using dipolar coupling measurements if the dynamics of the complex can be eliminated by freezing the sample at 100 K in the presence of a solvent (1,1,2,2-tetrachloroethane, TCE, in this case). As such we performed $^{13}C/^{15}N\{^{45}Sc\}$ RESPDOR experiments using DNP to help sensitize the difficult natural abundance experiments. These experiments enable for the measurement of the radial C-Sc and N-Sc distances in the complex, which in particular can help distinguish configuration **5** from the others. In contrast with the $^{1}H\{^{45}Sc\}$ RESPDOR experiments, here we used REDOR recoupling,[58] as opposed to $SR4^2_1$, due to its $\sqrt{2}$ larger dipolar scaling factor, which enables for the measurement of longer distances (see Figure 7a). The ^{13}C and ^{15}N CPMAS spectra, and their corresponding RESDOR data are shown in Figure 7. Three ^{13}C chemical shifts and a single ^{15}N chemical shift are observed. Smaller secondary resonances are also observed that increase in prominence with air exposure and were thus assigned to partial decomposition products. Importantly, the experiment conclusively showed that all ^{15}N sites in the sample are coordinated to scandium and as such structure **5** can be eliminated. We note that we cannot differentiate structures **2** or **4** on the basis of the aforementioned NMR experiments but we found **4** to be dynamically unstable through molecular dynamics simulations, converting to **5** within mere picoseconds. As such, it is likely that **2** is the dominant configuration for the grafted complex. Indeed, when taking the DFT-optimized structure for **2** directly for the calculation of the $^{13}C/^{15}N\{^{45}Sc\}$ RESPDOR dephasing curves we find a remarkable agreement with all four curves, further corroborating our conclusion that the complex grafts to form the monopodal complex **2**. Note also, that the rigidity of the complex under DNP conditions was confirmed through the acquisition of a DNP-enhanced $^{13}C\{^{1}H\}$ wPDLF experiment which showed that the only dynamic motions at play at 100 K are the methyl rotations (Figure 8).

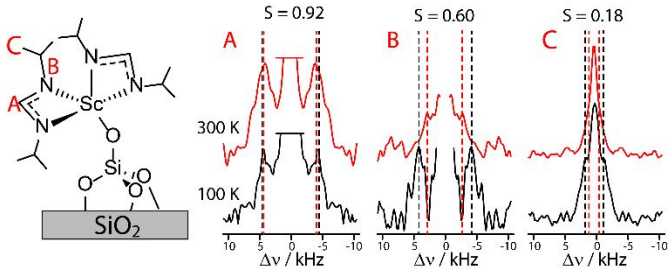

Figure 8. $^{13}C\{^{1}H\}$ wPDLF dipolar spectra of the grafted complex **2** (left). The spectra are labelled A-C using the structure of the left. The bottom spectra (black) were acquired at 100 K using DNP and in the presence of frozen TCE and demonstrate that the complex is rigid under these conditions, with the exception of methyl rotations. The top spectra (red) were acquired on a dry sample at room temperature and show the averaging of the *i*Pr ^{13}C-^{1}H dipolar coupling, by a factor of 0.60, due to molecular dynamics. The amidinate ligand as a whole (A) does not seem to undergo significant motions.

4.2.2. Dynamics

Having identified the configuration of the grafted complex produced when **1** was reacted with silica (**2**), it is of interest to analyze how this structure varies as a function of time and how these dynamics are contrasted by those observed for the molecular analogue **1**. To this end we performed a $^{13}C\{^1H\}$ wPDLF experiment at room temperature on the dry sample (see Figure 8). The experiment showed that the complex was rigidly bound to the silica surface with carbon 'A' having an order parameter of nearly 1 (see Table 2). As such, there was no evidence of significant Si-O or O-Sc rotations as have been previous noted in other silica-supported species.[42,43] The isopropyl groups, however, were themselves quite dynamic with order parameters in the range of 0.6 and the lineshape on the wPDLF spectrum suggesting that there may be several overlapping order parameters for this moiety, perhaps from the four different *i*Pr groups on a given metal complex. Importantly, the $\langle S \rangle$ value of 0.6 is far larger than the value of 0.33 that is expected in the case of a freely-rotating *i*Pr group, as was observed in the case of **1**, suggested that the rotations of the *i*Pr groups may be impeded by them coming into contact with the silica surface.

Table 2. Experimental and calculated dipolar order parameters.

sample	$\langle S \rangle$(amidinate)	$\langle S \rangle$(*i*Pr)	$\langle S \rangle(CH_3)$[a]	$\langle S \rangle$(Sc-amidinate)
1	0.12 ± 0.06	0.04 ± 0.03	<0.02	0.20 ± 0.03
2, expt.	0.92 ± 0.10	0.60 ± 0.06	0.18 ± 0.05	1.0 ± 0.1
2, MD	0.39, 0.41	0.13, 0.19, 0.23 0.25	0.04, 0.06, 0.08, 0.08	0.45, 0.47
2, MD[b]	1.00	0.52, 0.52, 0.60, 0.72	0.17, 0.17 0.20, 0.24	1.00

[a] The MD time trace was too short to produce a statistical methyl rotation and as such the calculated methyl order parameters were simply calculated as $\langle S \rangle(CH_3) = \langle S \rangle(i\text{Pr})/3$. [b]This corresponds to the same MD run albeit while only considering the rotations of the *i*Pr groups, fixing the $\langle S \rangle$ (amidinate) and $\langle S \rangle$(Sc-amidinate) values to 1.0.

The observation that the complex possesses rigid Si-O and O-Sc bonds is also corroborated by a $^1H\{^{45}Sc\}$ RESPDOR experiment which had a remarkable agreement with the predicted dephasing curve simulated assuming an order parameter $\langle S \rangle$ of 1 (Figure 9 and Table 2). Note that this order parameter is expected to be slightly larger than the ^1H-^{13}C order parameter from carbon 'A' as the distance between the two coupled spin is greater and requires larger amplitude motions to average. The ^{45}Sc NMR spectra are also temperature independent (Figure S5), indicating again that there are no reorientations of the Sc EFG tensor at room temperature.

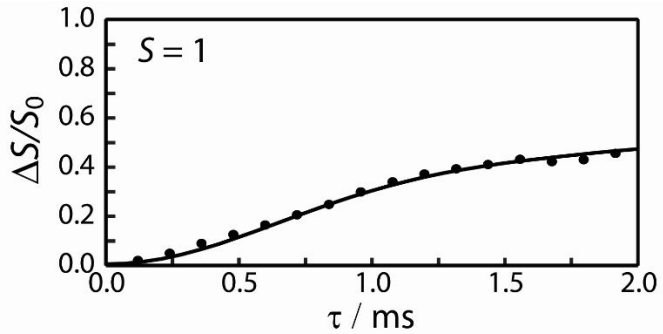

Figure 9. $^{1}H\{^{45}Sc\}$ RESPDOR dephasing curve acquired on the grafted complex **2**. Significant dephasing could only be observed for the amidinate ^{1}H. The simulated curve corresponds to an order parameter of 1, corroborating the $^{13}C\{^{1}H\}$ wPDLF observation that the amidinate ligands possess rigid orientations.

In order to interpret these data and gain a better understanding of the factors that influence the dynamics of the supported complex we performed DFT-based molecular dynamics calculations of **2**. The complex was allowed to freely evolve over a period of 100 ps over which the structure was stored every 10 fs, allowing for the calculation dipolar order parameters according to the procedure outlined in section 3.1. The averaging of the ^{1}H-^{45}Sc order parameter as well as the amidinate and *i*Pr ^{1}H-^{13}C order parameters are plotted as a function of the evolution time in Figure 10; a similar plot was calculated for **3** and is shown in Figure S9. Unlike experiment, the molecular dynamics simulations predict that the complex freely rotates about the bonds connecting it to the silica surface. In fact the order parameters predicted for the ^{1}H-^{45}Sc and ^{1}H-^{13}C dipolar couplings to the amidinate site decreased to 0.45 and 0.40, respectively (Table 2), far below the experimental values of 1.0 and 0.92 and even outpacing the mobility of the *i*Pr moieties that experimentally had order parameters in the range of 0.60.

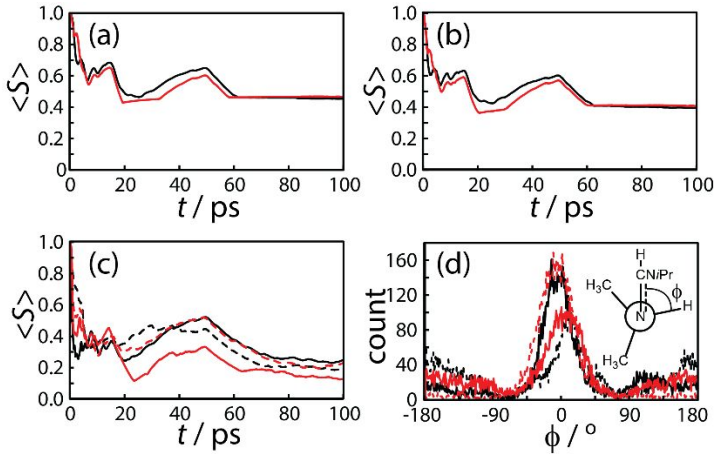

Figure 10. Results from the DFT-MD simulation of complex **2**. The order parameters for the ^{45}Sc-amidinate ^{1}H dipolar coupling (a), the amidinate $^{13}C\{^{1}H\}$ dipolar coupling (b), and *i*Pr $^{13}C\{^{1}H\}$ dipolar coupling (c) are shown as a function of the simulation time. The methyl $^{13}C\{^{1}H\}$ order parameters are not shown given that a longer simulation time is needed to perform full methyl rotations, instead it can be assumed to be 1/3 of the value in (c). Curves in red and black correspond to opposing ligands and the dashed and solid lines in (c) and (d) correspond to opposing *i*Pr moieties from the same ligand. In (d) the histograms of the *i*Pr-CH and amidinate N-C dihedral angle (ϕ) are shown.

To explain this finding, we hypothesized that the complex may be forming a second interaction with the surface to either a silanol (structure **4**) or a siloxane bridge. This last interaction has been postulated a number of times, particularly for d^0 metals such as Sc.[89,90,92-99] As such we DFT-optimized both of these structures onto an amorphous silica surface and proceeded to calculate their structural evolutions. The first complex (**4**) was found to rapidly convert to **5**

through the protonation of one of its amidinate ligands. Given that **5** can be disregarded based on our DNP-enhanced $^{13}C/^{15}N\{^{45}Sc\}$ RESPDOR measurements, structure **4** was thus also eliminated. The complex forming a dative interaction with a surface siloxane could be successfully optimized using DFT, indicating that it may be stable at 0 K. When a molecular dynamics calculation was performed at a temperature of 300 K, however, the complex was found to quickly break its siloxane-scandium bond, yielding a complex **2**, effecting once-again pronounced surface-metal rotations. As such, we found this bonding motif to also be kinetically unstable at experimentally-relevant temperatures (videos of the simulations are provided as supporting information). It is possible that the bulkier bidentate ligands found in this complex disfavor the formation of a weak siloxane-scandium dative interaction. Such interactions are also likely more probable in the case where the rotations of the complex are prevented through additional metal-surface interactions, as is the case for di- or tripodal complexes.[98]

Although it is difficult to say with certainty, it would appear that the restricted motions of the complex are of a steric nature. Most DFT calculations were performed on fairly flat substrates, while in reality the silica surface is far less uniform and could restrict the larger amplitude motions of the complex.[100] This is in agreement with prior work that has shown that the dynamics of silane functionalities are affected by the synthetic approach used to make the silica.[43] We have also attempted to release the complex and enable its free rotation by wetting it with benzene or 1,1,2,2-tetrachloroethane, and also by dehydroxylating the surface at a higher temperature of 700 °C. None of these experiments reduced the $^{1}H\{^{45}Sc\}$ RESPDOR dephasing rate, indicating that the complex remained rigidly confined on the surface (see supporting information).

If we analyze instead only the dynamics of the *i*Pr moieties of the ligands while disregarding the dynamics of the metal, we find that the molecular dynamics simulations are able to quantitatively reproduce the experimental order parameters. To do this, we extracted the H-C-C-H dihedral angle describing the orientation of the isopropyl group relative to the amidinate backbone. A histogram of this dihedral angle for all four *i*Pr groups on complex **2** is shown in Figure 10b, along with the definition of the angle in question. Generally, the moieties tend to minimize the steric interactions between the methyl groups and the amidinate, preferring dihedrals of 0° and 180°. Each ligand has a single *i*Pr group that is more dynamic and another that is more rigid, overwhelmingly preferring dihedrals near 0°. By averaging over this motion alone, the *i*Pr order parameter is increased to values ranging from 0.52 to 0.72, in agreement with the experimentally determined value of 0.60 (see Table 2). As such while molecular dynamics simulations did not reproduce the dynamics of the metal, it did successfully replicate the dynamics of the *i*Pr groups.

To better visualize the mobility of the *i*Pr groups, we can utilize the familiar thermal ellipsoids used in crystallography and, like crystallography, draw the ellipsoids covering a range with a 50% probability of finding the atom in question. The obtained thermal ellipsoids can be visualized in Figure 11 along with the static DFT-optimized structure of **2**. One of the two amidinate ligands can be seen to have more dynamic *i*Pr moieties. This ligand featured the most rearrangement in the molecular dynamics simulation and is located above a crevice in the silica surface. The other ligand would appear to have hindered *i*Pr dynamics presumably due to steric

interactions with the surface, in agreement with our hypothesis that these interactions may be responsible for limiting the dynamics of the complex.

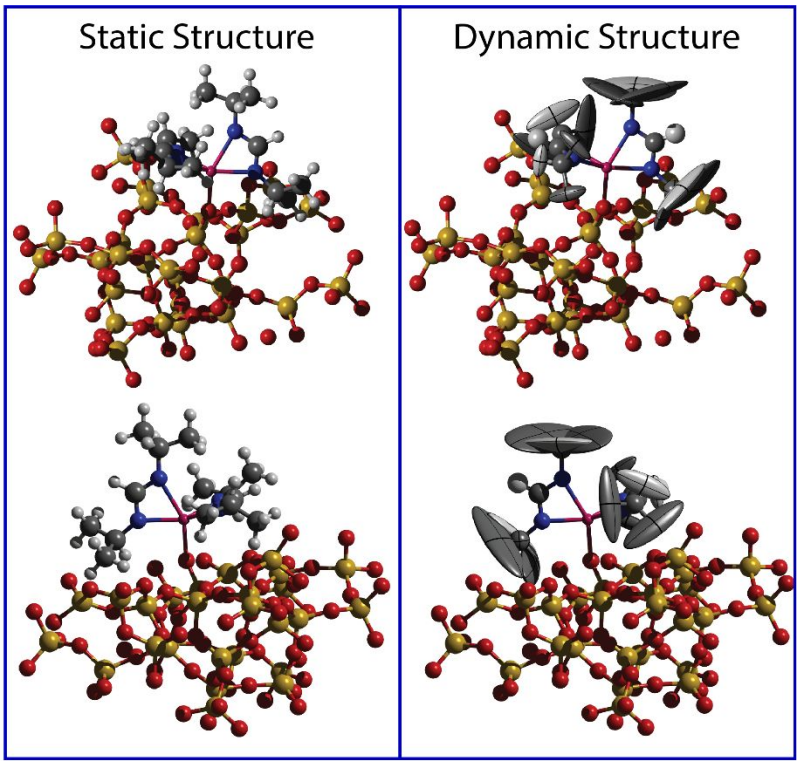

Figure 11. Three-dimensional depictions of the static, DFT-optimized and NMR-validated, structure of **2** (left) as well as its dynamic analogue (right), determined using a combination of dynamic NMR measurements and molecular dynamics simulations. Thermal ellipsoids are used to depict the available range of motions (right); methyl hydrogen atoms were removed for clarity. The ellipsoids correspond to the volume encompassing a 50% probability of finding the given atom.

5. Conclusions

We have investigated the dynamics of a scandium amidinate complex both in the molecular form in the crystal as well as grafted onto a silica surface using multinuclear and multidimensional solid-state NMR spectroscopy. The molecular complex was found to undergo nearly isotropic motions in the crystal with a cube-like reorientation symmetry. In addition, in this complex the order parameters for the *i*Pr moieties were found to be roughly 1/3 those of the central amidinate carbon, suggesting that they undergo free rotation.

^{1}H-^{1}H double-quantum correlation spectroscopy, ^{45}Sc MAS NMR, and DNP-enhanced ^{13}C/^{15}N{^{45}Sc} distance measurements were used, in combination with DFT, to determine the configuration of the grafted species. It was determined that it coordinates to the surface in a monopodal fashion and retained two of its original three amidinate ligands. Dynamic NMR experiments utilizing ^{1}H-^{13}C and ^{1}H-^{45}Sc dipolar coupling showed that unlike the molecular

species, the motions of the grafted species were severely hindered. The complex was not observed to undergo motion about its bond anchoring it to the surface and the only dynamics were those of the *i*Pr groups. These were also observed to have hindered rotations, having greater local order parameters than those measured in the free complex. Molecular dynamics calculations were applied to interpret the experimentally determined order parameters. The simulations performed on flat silica surfaces all led to the free rotation of the complex on the surface, in contrast with experiment. While we hypothesized that a secondary siloxane-metal interaction may be fixing the orientation of the complex, such an interaction was found to be kinetically unstable by molecular dynamics calculations and thus we conclude that the dynamics are likely restricted by steric interactions with the silica surface. Nevertheless, the molecular dynamics calculations were able to replicate the dynamics of the *i*Pr groups, enabling the experimental solution of a dynamic three-dimensional structure for a supported metal complex.

6. Acknowledgements

This work was supported by the U.S. Department of Energy (DOE), Office of Basic Energy Sciences, Division of Chemical Sciences, Geosciences, and Biosciences through a DOE Early Career Project (FAP and ALP). Molecular dynamics calculations (DJL) were supported by the Ames Laboratory Chemical Physics program and synthesis (ADS and UK) by the Ames Laboratory Catalysis program. Ames Laboratory is operated for the DOE by Iowa State University under Contract No. DE-AC02-07CH11358. Initial work for FAP was supported by an Ames Laboratory Laboratory-Directed Research and Development (LDRD) program.

7. References

[1] C. A. Tolman, Steric effects of phosphorus ligands in organometallic chemistry and homogeneous catalysis, *Chem. Rev.* 1977, **77**, 313-348.

[2] K. Angermund, W. Baumann, E. Dinjus, R. Fornika, H. Görls, M. Kessler, C. Krüger, W. Leitner, F. Lutz, Complexes [(P_2)Rh(hfacac)] as model compounds for the fragment [(P_2)Rh] and as highly active catalysts for CO_2 hydrogenation: The accessible molecular surface (AMS) model as an approach to quantifying the intrinsic steric properties of chelating ligands in homogeneous catalysis, *Chem. Eur. J.* 1997, **3**, 755-764.

[3] A. Poater, B. Cosenza, A. Correa, S. Giudice, F. Ragone, V. Scarano, L. Cavvallo, Samb*V*ca: A web application for the calculation of the buried volume of N-heterocyclic carbene ligands. *Eur. J. Inorg. Chem* 2009, 1759-1766.

[4] L. Cavallo, A. Correa, C. Costabile, H. Jacobsen, Steric and electronic effects in the bonding of N-heterocyclic ligands to transition metals, *J. Organomet. Chem.* 2005, **690**, 5407-5413.

[5] A. C. Hillier, W. J. Sommer, B. S. Yong, J. L. Petersen, L. Cavallo, S. P. Nolan, A combined experimental and theoretical study examining the binding of N-heterocyclic carbenes (NHC) to the Cp*RuCl (Cp*=η^5-C_5Me_5) moiety: Insight into stereoelectronic differences between unsaturated and saturated NHC ligands, *Organomet.* 2003, **22**- 4322-4326.

[6] B. S. Billow, T. J. McDaniel, A. L. Odom, Quantifying ligand effects in high-oxidation-state metal catalysis, *Nature Chem.* 2017, **9**, 837-842.

[7] K. Wu, A. G. Doyle, Parameterization of phosphine ligands demonstrates enhancement of nickel catalysis via remote steric effects, *Nature Chem.* 2017, **9**, 779-784.

[8] K. C. Harper, S. C. Vilardi, M. S. Sigman, Prediction of catalyst and substrate performance in the enantioselective propargylation of aliphatic ketones by a multidimensional model of steric effects, *J. Am. Chem. Soc.*, 2013, **135**, 2482-2485.
[9] K. B. Lipkowitz, C. A. D'Hue, T. Sakamoto, J. N. Stack, Stereocartography: A computational mapping technique that can locate regions of maximum stereoinduction around chiral catalysts, *J. Am. Chem. Soc.* 2002, **124**, 14255-14267.
[10] J. M. Smith, B. C. Taverner, N. J. Coville, Cone angle radial profiles, *J. Organomet. Chem.* 1997, **530**, 131-140.
[11] I. A. Guzei, M. Wendt, An improved method for the computation of ligand steric effects based on solid angles, *Dalton Trans.* 2006, 3991-3999.
[12] L. Falivene, R. Credendino, A. Poater, A. Petta, L. Serra, R. Oliva, V. Scarano, L. Cavallo, SambVca 2. A web tool for analyzing catalytic pockets with topographic steric maps, *Organometallics*, 2016, **35**, 2286-2293.
[13] P. Liu, J. Montgomery, K. N. Houk, Ligand steric contours to understand the effects of N-heterocyclic carbene ligands on the reversal of regioselectivity in Ni-catalyzed reductive couplings of alkynes and aldehydes, *J. Am. Chem. Soc.* 2011, **133**, 6956-6959.
[14] H. Wang, G. Liu, G. J. Sormunen, H. A. Malik, P. Liu, J. Montgomery, NHC ligands tailored for simultaneous regio- and enantiocontrol in nickel-catalyzed reductive couplings, *J. Am. Chem. Soc.* 2017, **139**, 9317-9324.
[15] L. Falivene, Z. Cao, A. Petta, L. Serra, A. Poater, R. Oliva, V. Scarano, L. Cavallo, Towards the online computer-aided design of catalytic pockets, *Nature Chem.* 2019, **11**, 872-879.
[16] W. S. Knowles, Asymmetric Hydrogenations (Nobel Lecture), *Angew. Chem. Int. Ed.* 2002, **41**, 1998-2007.
[17] J. Guo, H.-X. Zhou, Protein allostery and conformational dynamics. *Chem. Rev.* 2016, **116**, 6603-6515.
[18] J. Kraut, How do enzymes work? *Science*. 1988, **242**, 533-540.
[19] G. G. Hammes, How do enzymes really work? *J. Bio. Chem.* 2008, **283**, 22337-22346.
[20] A. Kohen, Role of dynamics in enzyme catalysis: Substantial versus semantic controversies. *Acc. Chem. Res.* 2015, **48**, 466-473.
[21] K. F. Kalz, R. Kraehnert, M. Dvoyashkin, R. Dittmeyer, R. Gläser, U. Krewer, K. Reuter, J.-D. Grunwaldt, Future challenges in heterogeneous catalysis: Understanding catalysts under dynamic reaction conditions, *ChemCatChem*. 2017, **9**, 17-29.
[22] K. Singh, A. Sarbajna, I. Dutta, P. Pandey, J. K. Bera, Hemilability-driven water activation: A Ni^{II} catalyst for base-free hydration of nitriles to amides, *Chem Eur. J.* 2017, **23**, 7761-7771.
[23] F. Ragone, A. Poater, L. Cavallo, Flexibility of N-heterocyclic carbene ligands in ruthenium complexes relevant to olefin metathesis and their impact in the first coordination sphere of the metal, *J. Am. Chem. Soc.* 2010, **132**, 4249-4258.
[24] H. Clavier, S. P. Nolan, Percent buried volume for phosphine and N-heterocyclic carbene ligands: steric properties in organometallic chemistry. *Chem. Commun.* 2010, **46**, 841-861.
[25] G. Altenhoff, R. Goddard, C. W. Lehmann, F. Glorius, Sterically demanding, bioxazoline-derived N-heterocyclic carbene ligands with restricted flexibility for catalysis, *J. Am. Chem. Soc.* 2004, **126**, 15195-15201.
[26] I. C. Stewart, D. Benitez, D. J. O'Leary, E. Tkatchouk, M. W. Day, W. A. Goddard III, R. H. Grubbs, Conformations of N-heterocyclic carbene ligands in ruthenium complexes relevant to olefin metathesis, *J. Am. Chem. Soc.* 2009, **131**, 1931-1938.

[27] L. Biancalana, G. Ciancaleoni, S. Zacchini, A. Monti, F. Marchetti, G. Pampaloni, Solvent-dependent hemilability of (2-diphenylphosphino)phenol in a Ru(II) para-cymene system, *Organometallics*, 2018, **37**, 1381-1391.

[28] G. Altenhoff, R. Goddard, C. W. Lehmann, F. Glorius, An N-heterocyclic carbene ligand with flexible steric bulk allows Suzuki cross-coupling of sterically hindered aryl chlorides at room temperature, *Angew. Chem. Int. Ed.* 2003, **42**, 3690-3693.

[29] C. Costabile, L. Cavallo, L. Origin of enantioselectivity in the asymmetric Ru-catalyzed metathesis of olefins, *J. Am. Chem. Soc.* 2004, **126**, 9592-9600.

[30] M. S. Jeletic, C. E. Lower, I. Ghiviriga, A. S. Veige, Chemical exchange saturation transfer (CEST) as a tool to measure ligand flexibility of chelating chiral di-N-heterocyclic carbene complexes, *Organometallics*, 2011, **30**, 6034-6043.

[31] D. P. Estes, C. P. Gordon, A. Fedorov, W.-C. Liao, H. Ehrhorn, C. Bittner, M. L. Zier, D. Bockfeld, K. W. Chan, O. Eisenstein, C. Raynaud, M. Tamm, C. Copéret, Molecular and silica-supported molybdenum alkyne metathesis catalysts: Influence of electronics and dynamics on activity revealed by kinetics, solid-state NMR, and chemical shift analysis, *J. Am. Chem. Soc.* 2017, **139**, 17597-17607.

[32] H. Zhai, A. N. Alexandrova, Local fluxionality of surface-deposited cluster catalysts: The case of Pt_7 on Al_2O_3, *J. Phys. Chem. Lett.* 2018, **9**, 1696-1702.

[33] H. Zhai, A. N. Alexandrova, Fluxionality of catalytic clusters: When it matters and how to address it, *ACS Catal.* 2017, **7**, 1905-1911.

[34] P. Berruyer, M. Lelli, M. P. Conley, D. L. Silverio, C. M. Widdifield, G. Siddiqi, D. Gajan, A. Lesage, C. Copéret, L. Emsley. Three-dimensional structure determination of surface sites, *J. Am. Chem. Soc.* 2017, **139**, 849-855.

[35] T. Maly, G. T. Debelouchina, V. S. Bajaj, K.-N. Hu, C.-G. Joo, M. L. Mak-Jurkauskas, J. R. Sirigiri, P. C. A. van der Wel, J. Herzfeld, R. J. Temkin, R. G. Griffin, Dynamic nuclear polarization at high magnetic fields, *J. Chem. Phys.* 2008, **128**, 052211.

[36] A. Lesage, M. Lelli, D. Gajan, M. A. Caporini, V. Vitzthum, P. Miéville, J. Alauzun, A. Roussey, C. Thieuleux, A. Mehdi, G. Bodenhaussen, C. Copéret, L. Emsley, Surface enhanced NMR spectroscopy by dynamic nuclear polarization, *J. Am. Chem. Soc.* 2010, **132**, 15459-15461.

[37] T. Kobayashi, F. A. Perras, I. I. Slowing, A. D. Sadow, M. Pruski, Dynamic nuclear polarization solid-state NMR in heterogeneous catalysis research, *ACS Catal.* 2015, **5**, 7055-7062.

[38] T. H. Walter, G. R. Frauenhoff, J. R. Shapley, E. Oldfield, Characterization of silica-supported osmium carbonyl clusters by magic-angle-spinning carbon-13 NMR spectroscopy, *Inorg. Chem.* 1991, **30**, 4732-4739.

[39] F. Engelke, S. Bhatia, T. S. King, M. Pruski, Dynamic hydrogen at the surface of supported ruthenium, *Phys Rev. B* 1994, **49**, 2730-2738.

[40] B. L. Moroz, I. L. Moudrakovski, V. A. Likholobov, Heterogenized catalysts for olefin hydroformylation containing cobalt and palladium-cobalt complexes anchored on phosphinated SiO_2: a ^{13}C solid-state NMR study, *J. Mol. Catal. A*, 1996, **112**, 217-233.

[41] J. O. Ehresmann, P. W. Kletnieks, A. Liang, V. A. Bhirud, O. P. Bagatchenko, E. J. Lee, M. Klaric, B. C. Gates, J. F. Haw, Evidence from NMR and EXAFS studies of a dynamically uniform mononuclear single-site zeolite-supported rhodium catalyst, *Angew. Chem. Int. Ed.* 2006, **45**, 574-576.

[42] F. Blanc, J.-M. Basset, C. Copéret, A. Sinha, Z. J. Tonzetich, R. R. Schrock, X. Solans-Monfort, E. Clot, O. Eisenstein, A. Lesage, L. Emsley, Dynamics of silica-supported catalysts determined

by combining solid-state NMR spectroscopy and DFT calculations, *J. Am. Chem. Soc.* 2008, **130**, 5886-5900.

[43] J. Gath, G. L. Hoatson, R. L. Vold, R. Berthoud, C. Copéret, M. Grellier, S. Sabo-Etienne, A. Lesage, L. Emsley, Motional heterogeneity in single-site silica-supported species revealed by deuteron NMR, *Phys. Chem. Chem. Phys.* 2009, **11**, 6962-6971.

[44] F. T. Edelmann, Lanthanide amidinates and guanidinates: from laboratory curiosities to efficient homogeneous catalysts and precursors for rare-earth oxide thin films, *Chem. Soc, Rev.* 2009, **38**, 2253-2268.

[45] S. V. Dvinskikh, H. Zimmermann, A. Maliniak, D. Sandström, Measurements of motionally averaged heteronuclear dipolar couplings in MAS NMR using R-type recoupling, *J. Magn. Reson.* 2004, **168**, 194-201.

[46] A. Gansmüller, J.-P. Simorre, S. Hediger, Windowed R-PDLF recoupling: A flexible and reliable tool to characterize molecular dynamics, *J. Magn. Reson.* 2013, **234**, 154-164.

[47] X. Zhao, M. Edén, M. H. Levitt, Recoupling of heteronuclear dipolar interactions in solid-state NMR using symmetry-based pulse sequences, *Chem. Phys. Lett.* 2001, **342**, 353-361.

[48] M. Edén, Enhanced symmetry-based dipolar recoupling in solid-state NMR, *Chem. Phys. Lett.* 2003, **378**, 55-64.

[49] Z. Gan, Measuring multiple carbon–nitrogen distances in natural abundant solids using R-RESPDOR NMR, *Chem Commun.* 2006, 4712-4714.

[50] A. Brinkmann, A. P. M. Kentgens, Proton-selective ^{17}O-^{1}H distance measurements in fast magic-angle-spinning solid-state NMR spectroscopy for the determination of hydrogen bond lengths, *J. Am. Chem. Soc.* 2006, **128**, 14758-14759.

[51] L. Chen, Q. Wang, B. Hu, O. Lafon, J. Trébosc, F. Deng, J.-P. Amoureux, Measurement of hetero-nuclear distances using a symmetry-based pulse sequence in solid-state NMR, *Phys. Chem. Chem. Phys.* 2010, **12**, 9395-9405.

[52] M. Feike, D. E. Demco, R. Graf, J. Gottwald, S. Hafner, H. W. Spiess, Broadband multiple-quantum NMR spectroscopy, *J. Magn. Reson., Ser. A*, 1996, **122**, 214-221.

[53] M. Rosay, L. Tometich, S. Pawsey, R. Bader, R. Schauwecker, M. Blank, P. M. Borchard, S. R. Cauffman, K. L. Felch, R. T. Weber, R. J. Temkin, R. G. Griffin, W. E. Maas, Solid-state dynamic nuclear polarization at 263 GHz: spectrometer design and experimental results, 2010, **12**, 5850-5960.

[54] A. Zagdoun, G. Casano, O. Ouari, M. Schwarzwälder, A. J. Rossini, F. Aussenac, M. Yulikov, G. Jeschke, C. Copéret, A. Lesage, P. Tordo, L. Emsley, Large molecular weight nitroxide biradicals providing efficient dynamic nuclear polarization at temperatures up to 200 K, *J. Am. Chem. Soc.* 2013, **135**, 12790-12797.

[55] A. Zagdoun, A. J. Rossini, D. Gajan, A. Bourdolle, O. Ouari, M. Rosay, W. E. Maas, P. Tordo, M. Lelli, L. Emsley, A. Lesage, C. Copéret, Non-aqueous solvents for DNP surface enhanced NMR spectroscopy, *Chem. Commun.* 2012, **48**, 654-656.

[56] T. Kobayashi, F. A. Perras, U. Chaudhary, I. I. Slowing, W. Huang, A. D. Sadow, M. Pruski, Improved strategies for DNP-enhanced 2D ^{1}H-X heteronuclear correlation spectroscopy of surfaces, *Solid State Nucl. Magn. Reson.* 2017, **87**, 38-44.

[57] T. Gullion, D. B. Baker, M. S. Conradi, New, compensated Carr-Purcell Sequences, *J. Magn. Reson.* 1990, **89**, 479-484.

[58] T. Gullion, J. Schaefer, Rotational-echo double-resonance NMR, *J. Magn. Reson.* 1989, **81**, 196-200.

[59] F. Pourpoint, J. Trébosc, R. M. Gauvin, Q. Wang, O. Lafon, F. Deng, J.-P. Amoureux, Measurement of aluminum-carbon distances using S-RESPDOR NMR experiments, *ChemPhysChem*, 2012, **13**, 3605-3615.
[60] S. J. Clark, M. D. Segall, C. J. Pickard, P. J. Hasnip, M. I. J. Probert, K. Refson, M. C. Payne, First principles methods using CASTEP, *Z. Kristall.* 2005, **220**, 567-570.
[61] C. J. Pickard, F. Mauri, F. All-electron magnetic response with pseudopotentials: NMR chemical shifts. *Phys. Rev. B.* 2001, **63**, 245101.
[62] J. R. Yates, C. J. Pickard, F. Mauri, Calculation of NMR chemical shifts for extended systems using ultrasoft pseudopotentials, *Phys. Rev. B.* 2007, **76**, 024401.
[63] J. P. Perdew, K. Burke, M. Ernzerhof, Generalized gradient approximation made simple, *Phys. Rev. Lett.* 1996, **77**, 3865-3868.
[64] D. Vanderbilt, Soft self-consistent pseudopotentials in a generalized eigenvalue formalism, *Phys. Rev. B*. 1990, **41**, 7892-7895.
[65] Comas-Vives, A. Amorphous SiO_2 surface models: energetics of the dehydroxylation process, strain, *ab initio* atomistic thermodynamics and IR spectroscopic signatures, *Phys. Chem. Chem. Phys.* 2016, **18**, 7475-7482.
[66] M. Profeta, M. Benoit, F. Mauri, C. J. Pickard, First-principles calculation of the ^{17}O NMR parameters in Ca oxide and Ca aluminosilicates: the partially covalent nature of the Ca−O bond, a challenge for density functional theory, *J. Am. Chem. Soc.* 2004, **126**, 12628-12635.
[67] A. Sadoc, M. Body, C. Legein, M. Biswal, F. Fayon, X. Rocquefelte, F. Boucher, NMR parameters in alkali, alkaline earth and rare earth fluorides from first principle calculations, *Phys. Chem. Chem. Phys.* 2011, **13**, 18539-18550.
[68] A. Jaworski, T. Charpentier, B. Stevensson, M. Edén, Scandium and yttrium environments in aluminosilicate glasses unveiled by $^{45}Sc/^{89}Y$ NMR spectroscopy and DFT calculations: What structural factors dictate the chemical shifts? *J. Phys. Chem. C*, 2017, **121**, 18815-18829.
[69] T. Charpentier, The PAW/GIPAW approach for computing NMR parameters: A new dimension added to NMR of solids. *Solid State Nucl. Magn. Reson.* 2011, **40**, 1-20.
[70] N. Kim, C.-H. Hsieh, J. F. Stebbins, Scandium coordination in solid oxides and stabilized zirconia: ^{45}Sc NMR. *Chem. Mater.* 2006, **18**, 3855-3859.
[71] G. Kresse, J. Hafner, Ab initio molecular dynamics for liquid metals, *Phys. Rev. B* 1993, **47**, R558-R561
[72] G. Kresse, J. Furthmüller, Efficiency of ab-initio total energy calculations for metals and semiconductors using a plane-wave basis set, *Comput. Mat. Sci.* 1996, **6**, 15-50.
[73] P. E. Blöchl, Projector augmented-wave method, *Phys. Rev. B*, 1994, **50**, 17953-17979.
[74] G. Kresse, D. Joubert, From ultrasoft pseudopotentials to the projector-augmented-wave method, *Phys. Rev. B*, 1999, **59**, 1758-1775.
[75] S. Nose, A unified formulation of the constant temperature molecular dynamics methods, *J. Chem. Phys.* 1984, **81**, 511-519.
[76] W. G. Hoover, Canonical dynamics: Equilibrium phase-space distributions, *Phys. Rev. A.* 1985, **31**, 1695-1697.
[77] R. E. Wasylishen, Dipolar and indirect coupling tensors in solids, in: Encyclopedia of Magnetic Resonance, 2007, John Wiley & Sons.
[78] S. Adiga, D. Aebi, D. L. Bryce, EFGShield — A program for parsing and summarizing the results of electric field gradient and nuclear magnetic shielding tensor calculations, *Can. J. Chem.* 2007, **85**, 496-505.

[79] Z. Pang, J. Zhang, W. Cao, X. Kong, X. Peng, Partitioning surface ligands on nanocrystals for maximal solubility, *Nature Commun.* 2019, **10**, 2454.
[80] T. Kobayashi, J. A. DiVerdi, G. E. Maciel, Silica gel surface: Molecular dynamics of surface silanols, *J. Phys. Chem. C* 2008, **112**, 4315-4326.
[81] F. A. Perras, U. Chaudhary, I. I. Slowing, M. Pruski, Probing surface hydrogen bonding and dynamics by natural abundance, multidimensional, ^{17}O DNP-NMR spectroscopy, *J. Phys. Chem. C* 2016, **120**, 11535-11544.
[82] P. P. Man, Quadrupolar interactions, in: Encyclopedia of Magnetic Resonance, 2007, John Wiley & Sons.
[83] R. W. Schurko, S. Wi, L. Frydman, Dynamic effects on the powder line shapes of half-integer quadrupolar nuclei: A solid-state NMR study of XO_4^-groups, *J. Phys. Chem. A* 2002, **106**, 51-62.
[84] P. Schanda, M. Ernst, Studying dynamics by magic-angle spinning solid-state NMR spectroscopy: Principles and applications to biomolecules, *Prog. Nucl. Magn. Reson. Spectrosc.* 2016, **96**, 1-46.
[85] X. Lu, H. Zhang, M. Lu, A. J. Vega, G. Hou, T. Polenova, Improving dipolar recoupling for site-specific structural and dynamics studies in biosolids NMR: windowed RN-symmetry sequences, *Phys. Chem. Chem. Phys.* 2016, **18**, 4035-4044.
[86] A. Ramamoorthy, Y. Wei, D.-K. Lee, PISEMA solid-state NMR spectroscopy, *Annu. Rep. NMR Spectrosc.* 2004, **52**, 1-52.
[87] M. G. Munowitz, R. G. Griffin, G. Bodenhausen, T. H. Huang, Two-dimensional rotational spin-echo nuclear magnetic resonance in solids: correlation of chemical shift and dipolar interactions, *J. Am. Chem. Soc.* 1981, **103**, 2529-2533.
[88] T. F. Kemp, M. E. Smith, QuadFit—A new cross-platform computer program for simulation of NMR line shapes from solids with distributions of interaction parameters *Solid State Nucl. Magn. Reson.* 2009, **35**, 243-252.
[89] T. Vancompernolle, X. Trivelli, L. Delevoye, F. Pourpoint, R. M. Gauvin, On the use of solid-state ^{45}Sc NMR for structural investigations of molecular and silica-supported scandium amide catalysts, *Dalton Trans.* 2017, **46**, 13176-13179.
[90] D. B. Culver, W. Huynh, H. Tafazolian, M. P. Conley, Solid-state ^{45}Sc NMR studies of $Cp^*_2Sc{-}OR$ (R = CMe_2CF_3,$CMe(CF_3)_2$, $C(CF_3)_3$, $SiPh_3$) and relationship to the structure of Cp^*_2Sc-sites supported on partially dehydroxylated silica, *Organometallics*, 2020, **39**, 1112-1122.
[91] P. Pyykkö, P. Year-2017 nuclear quadrupole moments. *Mol. Phys.* 2018, **116**, 1328-1338.
[92] J. Corker, F. Lefebvre, C. Lécuyer, V. Dufaud, F. Quignard, A. Choplin, J. Evans, J.-M. Basset, Catalytic cleavage of the C-H and C-C bonds of alkanes by surface organometallic chemistry: An EXAFS and IR characterization of a Zr-H catalyst, *Science*, 1996, **271**, 966-969.
[93] V. Vidal, A. Théolier, J. Thivolle-Cazat, J-M. Basset, J. Corker, Synthesis, characterization, and reactivity, in the C-H bond activation of cycloalkanes, of a silica-supported tantalum(III) monohydride complex: $(\equiv SiO)_2Ta^{III}$-H, *J. Am. Chem. Soc.* 1996, **118**, 4595-4602.
[94] C. Copéret, M. Chabanas, R. P. Saint-Arroman, J.-M. Basset, Homogeneous and heterogeneous catalysis: Bridging the gap through surface organometallic chemistry, *Angew. Chem. Int. Ed.* 2003, **42**, 156-181.

[95] M. Chabanas, A. Baudouin, C. Copéret, J.-M. Basset, W. Lukens, A. Lesage, S. Hediger, L. Emsley, Perhydrocarbyl Re^{VII} complexes : Comparison of molecular and surface complexes, *J. Am. Chem. Soc.* 2003, **125**, 492-504.

[96] R. M. Gauvin, A. Mortreux, Silica-supported lanthanide silylamides for methyl methacrylate polymerisation: controlled grafting induces controlled reactivity, *Chem Commun.* 2005, 1146-1148.

[97] R. M. Gauvin, L. Delevoye, R. A. Hassan, J. Keldenich, A. Mortreux, Well-defined silica-supported rare-earth silylamides, *Inorg. Chem.* 2007, **46**, 1062-1070.

[98] I. Del Rosal, I. C. Gerber, R. Poteau, L. Maron, Grafting lanthanide complexes on silica surfaces: A theoretical investigation, *J. Phys. Chem. A*, 2010, **114**, 6322-6330.

[99] T. Vancompernolle, A. Valente, T. Chenal, P. Zinck, I. Del Rosal, L. Maron, M. Taoufik, S. Harder, R. M. Gauvin, Silica-grafted lanthanum benzyl species: Synthesis, characterization, and catalytic applications, *Organometallics*, 2017, **36**, 3912-3920.

[100] B. Zandkarimi, T. J. Gorey, G. Li, J. Munarriz, S. L. Anderson, A. N. Alexandrova, Alloying with Sn suppresses sintering of size-selected subnano Pt clusters on SiO_2 with and without adsorbates, *Chem. Mater.* 2020, **32**, 8595-8605.